

Ground-state phases and spin textures of spin-orbit-coupled dipolar Bose-Einstein condensates in a rotating toroidal trap

Qing-Bo Wang(王庆波), Hui Yang(杨慧), Ning Su(苏宁), Ling-Hua Wen(文灵华)

Citation: Chin. Phys. B . 2020, 29(11): 116701 . **doi:** 10.1088/1674-1056/abbbe8
Journal homepage: http://cpb.iphy.ac.cn; http://iopscience.iop.org/cpb

What follows is a list of articles you may be interested in

Accelerate Bose-Einstein condensate by interaction

Jie-Li Qin(秦杰利)

Chin. Phys. B . 2019, 28(12): 126701 . **doi:** 10.1088/1674-1056/ab4e8a

Propagation of dark soliton interacting with domain wall in two immiscible Bose-Einstein condensates

Lang Zheng(郑浪), Yi-Cai Zhang(张义财), Chao-Fei Liu(刘超飞)

Chin. Phys. B . 2019, 28(11): 116701 . **doi:** 10.1088/1674-1056/ab457e

Expansion dynamics of a spherical Bose-Einstein condensate

Rui-Zong Li(李睿宗), Tian-You Gao(高天佑), Dong-Fang Zhang(张东方), Shi-Guo Peng(彭世国), Ling-Ran Kong(孔令冉), Xing Shen(沈星), Kai-Jun Jiang(江开军)

Chin. Phys. B . 2019, 28(10): 106701 . **doi:** 10.1088/1674-1056/ab4177

Spatiotemporal Bloch states of a spin-orbit coupled Bose-Einstein condensate in an optical lattice

Ya-Wen Wei(魏娅雯), Chao Kong(孔超), Wen-Hua Hai(海文华)

Chin. Phys. B . 2019, 28(5): 056701 . **doi:** 10.1088/1674-1056/28/5/056701

A space-dependent atomic superfluid current in Bose-Einstein condensates

Li Fei, Li Yong-Fan, Zhang Ping-Ke, Ai Zhen-Zhou, Wu Chang-Yi

Chin. Phys. B . 2015, 24(4): 046701 . **doi:** 10.1088/1674-1056/24/4/046701

Ground-state phases and spin textures of spin–orbit-coupled dipolar Bose–Einstein condensates in a rotating toroidal trap*

Qing-Bo Wang(王庆波)[1,2], Hui Yang(杨慧)[1,3], Ning Su(苏宁)[1], and Ling-Hua Wen(文灵华)[1,†]

[1] *Key Laboratory for Microstructural Material Physics of Hebei Province, School of Science, Yanshan University, Qinhuangdao* 066004, *China*
[2] *School of Physics and Technology, Tangshan Normal University, Tangshan* 063000, *China*
[3] *Department of Physics, Xinzhou Teachers University, Xinzhou* 034000, *China*

(Received 29 June 2020; revised manuscript received 17 August 2020; accepted manuscript online 28 September 2020)

We investigate the ground-state phases and spin textures of spin–orbit-coupled dipolar pseudo-spin-1/2 Bose–Einstein condensates in a rotating two-dimensional toroidal potential. The combined effects of dipole–dipole interaction (DDI), spin–orbit coupling (SOC), rotation, and interatomic interactions on the ground-state structures and topological defects of the system are analyzed systematically. For fixed SOC strength and rotation frequency, we provide a set of phase diagrams as a function of the DDI strength and the ratio between inter- and intra-species interactions. The system can show rich quantum phases including a half-quantum vortex, symmetrical (asymmetrical) phase with quantum droplets (QDs), asymmetrical segregated phase with hidden vortices (ASH phase), annular condensates with giant vortices, triangular (square) vortex lattice with QDs, and criss-cross vortex string lattice, depending on the competition between DDI and contact interaction. For given DDI strength and rotation frequency, the increase of the SOC strength leads to a structural phase transition from an ASH phase to a tetragonal vortex lattice then to a pentagonal vortex lattice and finally to a vortex necklace, which is also demonstrated by the momentum distributions. Without rotation, the interplay of DDI and SOC may result in the formation of a unique trumpet-shaped Bloch domain wall. In addition, the rotation effect is discussed. Furthermore, the system supports exotic topological excitations, such as a half-skyrmion (meron) string, triangular skyrmion lattice, skyrmion–half-skyrmion lattice, skyrmion–meron cluster, skyrmion–meron layered necklace, skyrmion–giant-skyrmion necklace lattice, and half-skyrmion–half-antiskyrmion necklace.

Keywords: Bose–Einstein condensate, dipole–dipole interaction, spin–orbit coupling, topological defects

PACS: 67.85.–d, 03.75.Kk, 03.75.Lm, 03.75.Mn **DOI:** 10.1088/1674-1056/abbbe8

1. Introduction

Many of the works in the field of ultracold quantum gases have focused on dipolar Bose–Einstein condensates (BECs) in the past few decades.[1,2] The dipole–dipole interaction (DDI), unlike the s-wave contact interaction, is long-range and anisotropic, which has significant influence on the stationary states, stability, and dynamic properties of ultracold atomic gases.[1–7] In addition, the DDI can be repulsive or attractive, and the tunability is crucial for systematically investigating new quantum states of dipolar BECs. In particular, recent experimental developments on atoms with large magnetic moments and polar molecules, such as the realization of BECs of ^{52}Cr,[8] ^{164}Dy,[9] and ^{168} Er[10] atoms, and the creation of ultracold molecules,[11] provide an opportunity to reveal more exotic properties of dipolar quantum gases and test the current theories on cold atom physics.

On the other hand, in recent years spin–orbit-coupled quantum gases have attracted great attention both experimentally and theoretically.[12–14] Spin–orbit coupling (SOC) describes the interaction between the spin and the momentum of a quantum particle, which is one of the key factors in determining the physics of the BEC system.[12] The SOC can be isotropic or anisotropic, including Rashba-type SOC,[15] Dresselhaus-type SOC,[16] the combination of Rashba SOC and Dresselhaus SOC,[17,18] and so on. In particular, recent experimental developments[19,20] on the realization of high-dimensional SOC have motivated a lot of investigations on high-dimensional topological matter both in theory and experiment. Relevant studies show that the BECs with SOC can exhibit many novel quantum phases and rich topological structures, such as plane-wave phase,[14,21] heliciform-stripe phase,[22] topological superfluid phase,[19] supersolid phase,[23] soliton excitation,[24] lattice phase,[25] half-quantum vortex, and skyrmion.[26–30] In a realistic physical system, ultracold quantum gases are trapped in an external potential. As a matter of fact, various external potentials can significantly affect the quantum states and dynamic properties of the BECs,[23,31–33] which results in rich physics. Recently, a novel non-simply connected external potential, i.e., a toroidal trap, has become experimentally achievable owing to

*Project supported by the National Natural Science Foundation of China (Grant Nos. 11475144 and 11047033), the Natural Science Foundation of Hebei Province, China (Grant Nos. A2019203049 and A2015203037), the University Science and Technology Foundation of Hebei Provincial Department of Education, China (Grant No. Z2017056), Science and Technology Plan Projects of Tangshan City, China (Grant No. 19130220g), and Research Foundation of Yanshan University, China (Grant No. B846).

†Corresponding author. E-mail: linghuawen@ysu.edu.cn

© 2020 Chinese Physical Society and IOP Publishing Ltd

the development of different techniques.[34] The toroidal trap sustains nontrivial topological configurations, exotic quantum dynamics, and precisely tunable features.[22,34–37]

In this work, we study the ground-state phases and spin textures of pseudo-spin-1/2 BECs with DDI and SOC in a rotating two-dimensional (2D) toroidal trap. We focus primarily on the combined effects of DDI, SOC, rotation, and contact interactions on the topological structures and properties of the system. For the case of fixed SOC strength and rotation frequency, we provide a set of phase diagrams with respect to the DDI strength and the contact interaction ratio. Particularly, the system shows novel quantum droplets (QDs)[38–40] resulted from repulsive DDI and repulsive contact interactions. In addition, the system displays rich vortex structures, such as triangular vortex lattice with QDs, square vortex lattice with QDs, criss-cross vortex string lattice, and vortex necklace, due to the interplay of DDI, SOC, and rotation. It is shown that the increase of SOC strength or rotation frequency can trigger a structural phase transition of the system, such as from an asymmetrical segregated phase with hidden vortices to a tetragonal vortex lattice then to a pentagonal vortex lattice and finally to a vortex necklace. Furthermore, the system sustains exotic spin textures and topological excitations including a trumpet-shaped spin Bloch domain wall, a half-skyrmion (meron) string, triangular skyrmion lattice, skyrmion–half-skyrmion lattice, skyrmion–meron cluster, skyrmion–meron layered necklace, skyrmion–giant-skyrmion necklace lattice, and half-skyrmion–half-antiskyrmion necklace.

The paper is organized as follows. The theoretical model for the system is introduced in Section 2. In Section 3, we present and analyze the ground-state phases and typical spin textures of the system. The effects of the DDI, SOC, and rotation frequency on the topological structures and properties of the system are systematically discussed. Our main findings are summarized in Section 4.

2. Model

We consider a quasi-2D system of pseudo-spin-1/2 BEC with DDI and Rashba SOC in a rotating 2D toroidal trap. In the mean-field approximation, the static and dynamic properties of such a system are governed by the generalized coupled Gross–Pitaevskii (GP) equations[1,12,14,41,42]

$$\begin{aligned}
\mathrm{i}\hbar\frac{\partial\psi_1}{\partial t} &= \Big[-\frac{\hbar^2\nabla^2}{2m}+V(\boldsymbol{r})+g_{11}|\psi_1|^2 \\
&\quad +g_{12}|\psi_2|^2-\Omega L_z\Big]\psi_1+\hbar(\lambda_x\partial_x-\mathrm{i}\lambda_y\partial_y)\psi_2 \\
&\quad +\Big(C_{\mathrm{dd}}^{11}\int U_{\mathrm{dd}}\left|\psi_1(\boldsymbol{r}',t)\right|^2\mathrm{d}\boldsymbol{r}' \\
&\quad +C_{\mathrm{dd}}^{12}\int U_{\mathrm{dd}}\left|\psi_2(\boldsymbol{r}',t)\right|^2\mathrm{d}\boldsymbol{r}'\Big)\psi_1, \qquad (1)
\end{aligned}$$

$$\begin{aligned}
\mathrm{i}\hbar\frac{\partial\psi_2}{\partial t} &= \Big[-\frac{\hbar^2\nabla^2}{2m}+V(\boldsymbol{r})+g_{21}|\psi_1|^2 \\
&\quad +g_{22}|\psi_2|^2-\Omega L_z\Big]\psi_2-\hbar(\lambda_x\partial_x+\mathrm{i}\lambda_y\partial_y)\psi_1 \\
&\quad +\Big(C_{\mathrm{dd}}^{21}\int U_{\mathrm{dd}}\left|\psi_1(\boldsymbol{r}',t)\right|^2\mathrm{d}\boldsymbol{r}' \\
&\quad +C_{\mathrm{dd}}^{22}\int U_{\mathrm{dd}}\left|\psi_2(\boldsymbol{r}',t)\right|^2\mathrm{d}\boldsymbol{r}'\Big)\psi_2. \qquad (2)
\end{aligned}$$

Here ψ_1 and ψ_2 denote the component wave functions of spin-up and spin-down, and the two component atoms have the same mass m. The system satisfies the normalization condition $\int[|\psi_1|^2+|\psi_2|^2]\mathrm{d}x\mathrm{d}y=N$, where N is the number of atoms. $V(\boldsymbol{r})$ is the external 2D toroidal potential, which can be expressed as[22,43]

$$\begin{aligned}
V(\boldsymbol{r}) &= \frac{1}{2}m\omega_\perp^2\left[V_0\left(\frac{r^2}{a_0}-a_0r_0\right)^2\right] \\
&= \frac{1}{2}\hbar\omega_\perp\left[V_0\left(\frac{r^2}{a_0^2}-r_0\right)^2\right]. \qquad (3)
\end{aligned}$$

Here $\omega_\perp$ is the radial oscillation frequency, $a_0=\sqrt{\hbar/m\omega_\perp}$, and $r=\sqrt{x^2+y^2}$. V_0 and r_0 are dimensionless parameters which characterize the central height and the width of the toroidal trap. The coefficients $g_{jj}=2\sqrt{2\pi}a_j\hbar^2/ma_z$ $(j=1,2)$ and $g_{12}=g_{21}=2\sqrt{2\pi}a_{12}\hbar^2/ma_z$ describe the intra- and interspecies interaction strengths, which are related to the s-wave scattering lengths a_j and a_{12} between intra- and inter-component atoms, and $a_z=\sqrt{\hbar/m\omega_z}$ is the oscillation length in the z direction. Ω is the rotation frequency along the z-direction, and $L_z=-\mathrm{i}\hbar(x\partial_y-y\partial_x)$ is the z component of the angular-momentum operator. λ_x and λ_y are the SOC strengths along the x- and y-directions, respectively. In the present work we only consider the case of isotropic Rashba SOC, i.e., $\lambda_x=\lambda_y=\lambda$. $C_{\mathrm{dd}}^{jj}=\mu_0\mu_j^2/4\pi$ $(j=1,2)$ and $C_{\mathrm{dd}}^{12}=C_{\mathrm{dd}}^{21}=\mu_0\mu_1\mu_2/4\pi$ are the magnetic DDI constants of intraspecies and interspecies, respectively. μ_0 is the magnetic permeability in vacuum, and μ_j $(j=1,2)$ is the magnetic dipole moment of the j-th component atom. Note that here we assume $\mu_1=\mu_2=\mu$, which means $C_{\mathrm{dd}}^{11}=C_{\mathrm{dd}}^{22}=C_{\mathrm{dd}}^{12}=C_{\mathrm{dd}}^{21}=C_{\mathrm{dd}}=\mu_0\mu^2/4\pi$. The 3D dipolar length is defined as $a_{\mathrm{dd}}^{\mathrm{3D}}=C_{\mathrm{dd}}m/3\hbar^2=\mu_0\mu^2m/12\pi\hbar^2$, and the 2D dipolar length is given by $a_{\mathrm{dd}}=\mu_0\mu^2mN/3\sqrt{2\pi}\hbar^2a_z$. Conventionally, we can define a ratio to characterize the relative strength of the DDI and the s-wave interaction,[1,2] $\gamma_{\mathrm{dd}}\equiv a_{\mathrm{dd}}/a_s=\mu_0\mu^2mN/3\sqrt{2\pi}\hbar^2a_z/a_{\mathrm{s}}$, where a_{s} is the s-wave scattering length.

The long-range and nonlocal DDI potential is given by[1,41]

$$U_{\mathrm{dd}}(\boldsymbol{r}-\boldsymbol{r}')=\frac{1-3\cos^2\theta}{|\boldsymbol{r}-\boldsymbol{r}'|^3}, \qquad (4)$$

where θ is the angle between the polarization direction and the relative position of the atoms. For the sake of numerical simulation, the DDI can be treated by Fourier transformation in k-space (momentum space) using a convolution theorem,[1,2,42] which is expressed as

$$\Phi(\boldsymbol{r},t)=\frac{\mu_0\mu^2 mN}{3\sqrt{2\pi}\hbar^2 a_z}\mathcal{F}_{2\mathrm{D}}^{-1}[\tilde{n}(\boldsymbol{k},t)F(\boldsymbol{k}a_z/\sqrt{2})]. \tag{5}$$

Here $\mathcal{F}_{2\mathrm{D}}$ is the 2D Fourier transform operator, i.e., $\widetilde{n}(\boldsymbol{k},t)=\mathcal{F}_{2\mathrm{D}}[n(\boldsymbol{r},t)]$. The function $F(\boldsymbol{q})$ with $\boldsymbol{q}\equiv\boldsymbol{k}a_z/\sqrt{2}$ is the k-space DDI for the quasi-2D geometry, which consists of two parts, resulting from polarization perpendicular or parallel to the direction of the dipole tilt. Concretely, $F(\boldsymbol{q})=\cos^2(\alpha)F_\perp(\boldsymbol{q})+\sin^2(\alpha)F_\parallel(\boldsymbol{q})$ with α being the angle between the z-axis and the polarization vector $\hat{\boldsymbol{d}}$. Here, $F_\perp(\boldsymbol{q})=2-3\sqrt{\pi}q\mathrm{e}^{q^2}\mathrm{erfc}(q)$, $F_\parallel(\boldsymbol{q})=-1+3\sqrt{\pi}(q_d^2/q)\mathrm{e}^{q^2}\mathrm{erfc}(q)$, q_d is the wave vector along the direction of the projection of $\hat{\boldsymbol{d}}$ onto the x–y plane, and erfc is the complementary error function. When the polarization is perpendicular to the condensate plane, i.e., $\alpha=0$, one can obtain $F(\boldsymbol{q})=2-3\sqrt{\pi}q\mathrm{e}^{q^2}\mathrm{erfc}(q)$, which has been discussed in previous work.[44] Here we assume that the polarization is parallel to the condensate plane, i.e., $\alpha=\pi/2$, thus $F(\boldsymbol{q})=-1+3\sqrt{\pi}(q_d^2/q)\mathrm{e}^{q^2}\mathrm{erfc}(q)$ in the present work.

By introducing the dimensionless parameters via notations $\widetilde{r}=r/a_0$, $\widetilde{t}=\omega_\perp t$, $\widetilde{V}(r)=V(r)/\hbar\omega_\perp$, $\widetilde{\Omega}=\Omega/\omega_\perp$, $\widetilde{L}_z=L_z/\hbar$, $\widetilde{\psi}_j=\psi_j a_0/\sqrt{N}$ $(j=1,2)$, $\beta_{jj}=g_{jj}N/\hbar\omega_\perp a_0^2$ $(j=1,2)$, and $\beta_{12}=\beta_{21}=g_{12}N/\hbar\omega_\perp a_0^2$, we obtain the dimensionless coupled GP equations for the dynamics of the system

$$\begin{aligned}\mathrm{i}\partial_t\psi_1 &= \left(-\frac{1}{2}\nabla^2+V+\beta_{11}|\psi_1|^2+\beta_{12}|\psi_2|^2-\Omega L_z+\Phi\right)\psi_1\\ &\quad+\lambda(\partial_x-\mathrm{i}\partial_y)\psi_2, \qquad (6)\\ \mathrm{i}\partial_t\psi_2 &= \left(-\frac{1}{2}\nabla^2+V+\beta_{12}|\psi_1|^2+\beta_{22}|\psi_2|^2-\Omega L_z+\Phi\right)\psi_2\\ &\quad-\lambda(\partial_x+\mathrm{i}\partial_y)\psi_1, \qquad (7)\end{aligned}$$

where the tilde is omitted for simplicity.

In order to describe the spacial distribution of the topological structure, we adopt a nonlinear Sigma model,[45] in which a normalized complex-valued spinor $\chi=[\chi_1,\chi_2]^{\mathrm{T}}$ with $|\chi_1|^2+|\chi_2|^2=1$ is introduced. The total density of the system is expressed by $\rho=|\psi_1|^2+|\psi_2|^2$, where the corresponding two-component wave functions are $\psi_1=\sqrt{\rho}\chi_1$ and $\psi_2=\sqrt{\rho}\chi_2$, respectively. The spin density is given by $\boldsymbol{S}=\overline{\chi}\sigma\chi$, where $\sigma=(\sigma_x,\sigma_y,\sigma_z)$ are the Pauli matrices, and the components of $\boldsymbol{S}$ are expressed as[30]

$$\begin{aligned}S_x &= \chi_1^*\chi_2+\chi_2^*\chi_1, \qquad (8)\\ S_y &= \mathrm{i}(\chi_2^*\chi_1-\chi_1^*\chi_2), \qquad (9)\\ S_z &= |\chi_1|^2-|\chi_2|^2, \qquad (10)\end{aligned}$$

with $|\boldsymbol{S}|=\sqrt{S_x^2+S_y^2+S_z^2}=1$. The spacial distribution of the topological structure of the system is described by the topological charge density

$$q(r)=\frac{1}{4\pi}\boldsymbol{S}\cdot\left(\frac{\partial\boldsymbol{S}}{\partial x}\times\frac{\partial\boldsymbol{S}}{\partial y}\right), \tag{11}$$

then we can obtain the topological charge Q by calculating the whole space integral of $q(r)$

$$Q=\int q(r)\mathrm{d}x\mathrm{d}y. \tag{12}$$

3. Results and discussion

For such a complex system, it is too difficult to obtain the analytical solutions. So we numerically solve the GP equations (6) and (7) and obtain the ground state of the system by using the imaginary-time propagation method.[21,46,47] In our calculation, we consider two-component BECs of ^{164}Dy[9,48,49] atoms with total atom number $N=500$. The trapping frequencies are assumed to be $(\omega_\perp,\omega_z)=2\pi\times(10,100)$ Hz, and the length scale is $a_0=2.483$ μm. The numerical discrete grids are chosen as 256×256, and the corresponding actual system is set as $10\times10{a_0}^2$. For convenience, we introduce a ratio between inter- and intra-species interactions, i.e., $\delta=\beta_{12}/\beta_{11}$. Without loss of generality, we assume that $\delta>1$ (initial component separation), $\beta_{11}=\beta_{22}=50$ with $a_{11}=29.6a_{\mathrm{B}}$ (a_{B} being the Bohr radius), $V_0=0.5$, and $r_0=3$, which are basically in agreement with the relevant parameters in experiment of BECs. It is shown that the system can display intriguing properties which are inaccessible in other systems.

3.1. The effect of DDI

We first study the effect of DDI on the ground-state configuration of the system with fixed SOC strength and rotation frequency. Considering the tunability of DDI and the competition between DDI and contact interaction, we provide a set of phase diagrams as a function of the DDI strength and the ratio between inter- and intra-species interactions (γ_{dd}–δ phase diagrams, see Figs. 1 and 3). Typical density distributions and phase distributions are displayed in Figs. 2 and 4.

In the repulsive DDI case ($\gamma_{\mathrm{dd}}>0$), the ground-state phases are classified into five types of stable phases (see Fig. 1), i.e., (I) half-quantum vortex (clockwise rotation) phase (HQV phase), (II) asymmetrical phase with quantum droplets (AQD phase), (III) symmetrical phase with quantum droplets (SQD phase), (IV) asymmetrical segregated phase with hidden vortices (ASH phase), and (V) annular condensates with giant vortices (ACG phase). When δ is small ($0<\delta\leq1$), the ground-state phase is almost a ACG phase (see Fig. 2(a)). In the regime of $1<\delta\leq4$, the region of ACG phase reduces gradually. At the same time, with the increase of γ_{dd}, the system displays a novel SQD phase (see Fig. 2(b)) or AQD

phase (see Fig. 2(c)). The only difference between them is the symmetry with respect to the x axis and the y axis, so we use dotted lines instead of solid lines to separate the identified regions. Here the quantum droplets[38–40] are mainly stabilized by the quantum many-body effects of the rotating spin–orbit-coupled dipolar BEC, especially by the competition between the repulsive DDI and the repulsive contact interaction. For large contact interaction ($4 < \delta < 8$), with the increase of the DDI strength the system undergoes a sequence of phase transitions from the ASH phase (see Fig. 2(d)) to the SQD phase, and then to the AQD phase or the HQV phase (see Fig. 2(e)). When the DDI strength exceeds a critical value ($\gamma_{dd} \geq 1$), the BEC system collapses.[1]

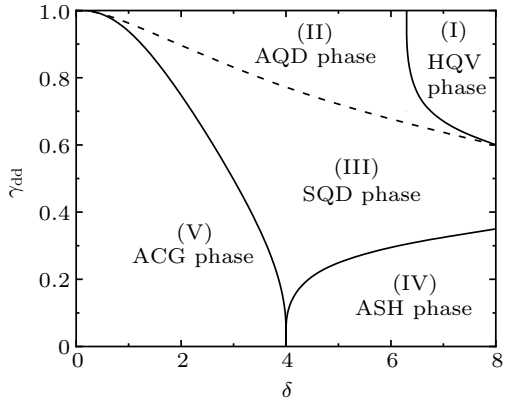


Fig. 1. The γ_{dd}–δ phase diagram with $\gamma_{dd} > 0$, $\Omega = 0.4$, and $\lambda = 1.5$. There are five different ground-state phases marked by (I)–(V). (I) half-quantum vortex phase (HQV phase), (II) asymmetrical phase with quantum droplets (AQD phase), (III) symmetrical phase with quantum droplets (SQD phase), (IV) asymmetrical segregated phase with hidden vortices (ASH phase), and (V) annular condensates with giant vortices (ACG phase). The unit length is a_0.

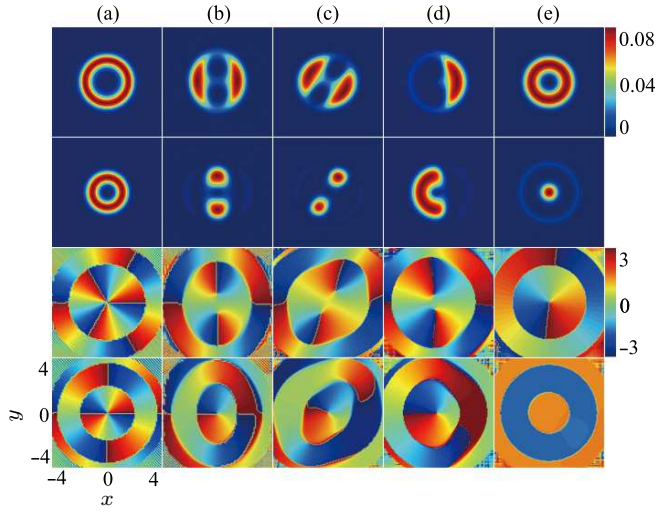


Fig. 2. Density distributions and phase distributions for different repulsive γ_{dd} with $\Omega = 0.4$ and $\lambda = 1.5$: (a) $\gamma_{dd} = 0.5$, $\delta = 1.7$, (b) $\gamma_{dd} = 0.5$, $\delta = 4$, (c) $\gamma_{dd} = 0.85$, $\delta = 6$, (d) $\gamma_{dd} = 0.15$, $\delta = 7.5$, and (e) $\gamma_{dd} = 0.65$, $\delta = 7.5$. The rows from top to bottom represent $|\psi_1|^2$, $|\psi_2|^2$, $\arg\psi_1$, and $\arg\psi_2$, respectively. The unit length is a_0.

In the attractive DDI case ($\gamma_{dd} < 0$), one can see that there are five main identified regions in Fig. 3, including (I) annular condensates with giant vortices (ACG phase), (II) triangular vortex lattice with quantum droplets (TVD phase), (III) square vortex lattice with quantum droplets (SVD phase), (IV) criss-cross vortex string lattice (CVS phase), and (V) triangular vortex lattice (TVL phase). In the regime of $0 < \delta < 4$, the system evolves from a SVD phase (Fig. 4(a)) into a TVL phase (Fig. 4(b)) as the attractive DDI strength increases (the absolute value of DDI increases). In the regime of $4 \leq \delta < 8$, the system undergoes a sequence of phase transitions: ACG phase (Fig. 4(c))→TVD phase (Fig. 4(d))→SVD phase→CVS phase (Fig. 4(e)) →TVL phase, with the increase of the attractive DDI strength. When the absolute value of DDI is larger than 7 ($\gamma_{dd} < -7$), the system remains in the TVL phase, where the density and phase distributions are similar to those in Fig. 4(b).

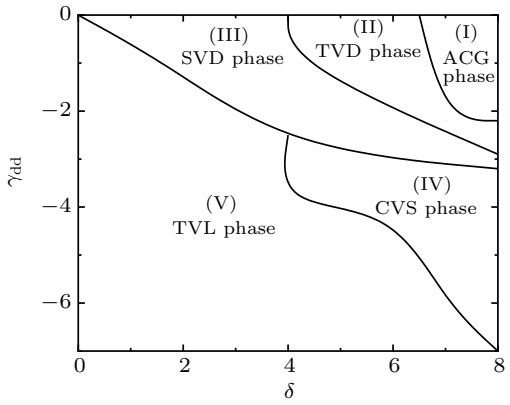


Fig. 3. The γ_{dd}–δ phase diagram with $\gamma_{dd} < 0$, $\Omega = 0.4$, and $\lambda = 1.5$. There are five different ground-state phases marked by (I)–(V). (I) annular condensates with giant vortices (ACG phase), (II) triangular vortex lattice with quantum droplets (TVD phase), (III) square vortex lattice with quantum droplets (SVD phase), (IV) criss-cross vortex string lattice (CVS phase), and (V) triangular vortex lattice (TVL phase). The unit length is a_0.

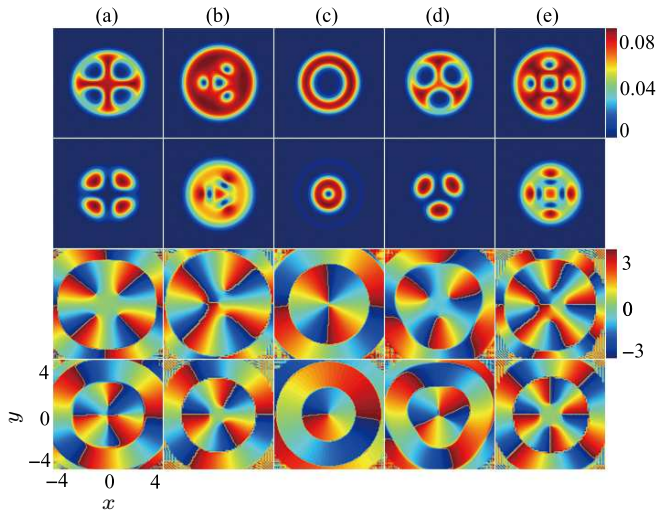


Fig. 4. Density distributions and phase distributions for different attractive γ_{dd} with $\Omega = 0.4$ and $\lambda = 1.5$: (a) $\gamma_{dd} = -3$, $\delta = 7.5$, (b) $\gamma_{dd} = -6$, $\delta = 4$, (c) $\gamma_{dd} = -2$, $\delta = 7.5$, (d) $\gamma_{dd} = -2.5$, $\delta = 7.5$, and (e) $\gamma_{dd} = -3$, $\delta = 4$. The rows from top to bottom represent $|\psi_1|^2$, $|\psi_2|^2$, $\arg\psi_1$, and $\arg\psi_2$, respectively. The unit length is a_0.

In short, rich topological structures can be obtained due to the effect of DDI, which plays an important role in the

BEC system. In particular, by tuning the DDI strength, novel topological states with QDs can be observed for fixed SOC strength and rotation frequency. It is found that the repulsive DDI with medium strength may lead to symmetric topological structures when the ratio δ is between 4 and 8. Therefore, we take $\gamma_{dd} = 0.5$ as one of the fixed parameters in the following numerical experiments.

3.2. The effect of SOC

Next we proceed to investigate the effect of SOC on the ground state of the system with fixed DDI strength and rotation frequency. As mentioned earlier, here we only consider the case of isotropic Rashba SOC. By varying the strength of SOC, the system can exhibit exotic topological structures. The typical density distributions, phase distributions, and momentum distributions (k-space densities) are displayed in Fig. 5. The rows from top to bottom represent $|\psi_1|^2$, $|\psi_2|^2$, $\arg\psi_1$, $\arg\psi_2$, and momentum distribution of component 2, respectively. The left four columns correspond to $\delta = 4$, and the right four columns correspond to $\delta = 7.5$.

As shown in Fig. 5(a), in the absence of SOC, i.e., $\lambda = 0$, the ground state of the system is phase separated (immiscible), consisting of a crescent density block and a bean-shaped density block. The component densities and phases are symmetric and antisymmetric with respect to the x axis, respectively. The loss of symmetry between the two separated component densities is mainly due to the anisotropic DDI and the strong interspecies repulsion. One can see that there are several hidden vortices[31,46,47] in each component which are essentially created by the interplay of rotation and repulsive contact interactions. At the same time, the density difference between the two components forms a combined crescent and bean structure, which leads to the generation of a unique trumpet-shaped spin Bloch domain wall (see Fig. 7(c)). In addition, the atoms are condensed in a narrow momentum regime with very finite momentum as shown in the momentum distribution of component 2 (see the bottom panel in Fig. 5(a)). Once the SOC is included, as shown in Fig. 5(b), the system shows an exotic square vortex lattice phase where the vortices in each component are arranged into a square lattice and the center of the trap for component 1 is occupied by an additional vortex. A deeper physical insight about the mechanism of the square vortex lattice can be obtained from its momentum distribution, which is presented in the bottom panel of Fig. 5(b). One can see that four momentum density peaks appear and approximately form a parallelogram around a ring. The square vortex lattice phase hence results from the combination of two pairs of plane waves with opposite momenta. The similar annular momentum distributions with multiple maxima have also been observed in a lattice phase of a non-rotating BEC with SOC in a harmonic trap[25] and in a metastable triangular stripe phase (or an annular vortex lattice state) of a BEC with SOC in a non-rotating (rotating) toroidal trap.[35] With the increase of the SOC strength, we can see that the number of vortices increases evidently and the vortices in the condensate tend to form a vortex necklace along a circle, where the density hole in the central region of each component is occupied by a singly quantized vortex or a hidden giant vortex (a hidden multiply quantized vortex) or a hidden vortex lattice (see Figs. 5(c) and 5(d)).[31,46,47] Interestingly, the maxima in the momentum distribution increase accordingly and the momentum-space densities exhibit similar structures to the real-space densities, as shown in the bottom row of Fig. 5.

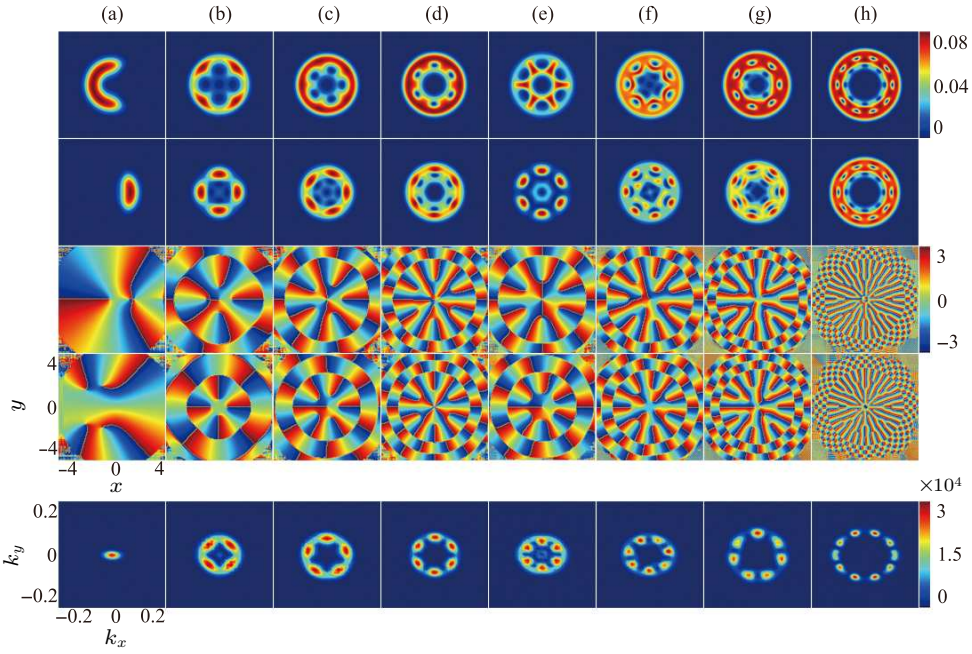


Fig. 5. Density distributions and phase distributions for different isotropic SOC strength λ with $\Omega = 0.8$ and $\gamma_{dd} = 0.5$: (a) $\lambda = 0$, $\delta = 4$, (b) $\lambda = 1.5$, $\delta = 4$, (c) $\lambda = 2$, $\delta = 4$, (d) $\lambda = 3$, $\delta = 4$, (e) $\lambda = 2$, $\delta = 7.5$, (f) $\lambda = 3$, $\delta = 7.5$, (g) $\lambda = 4$, $\delta = 7.5$, and (h) $\lambda = 10$, $\delta = 7.5$. The rows from top to bottom represent $|\psi_1|^2$, $|\psi_2|^2$, $\arg\psi_1$, $\arg\psi_2$, and momentum distribution of component 2, respectively.

For larger interspecies interaction, e.g., $\delta = 7.5$, the SOC effect becomes more pronounced. When the SOC strength is small, e.g., $\lambda = 2$, the system shows a complete phase separation and a novel hexagonal vortex lattice with petal-like quantum droplets, where a doubly quantized vortex is generated in the central region of component 1 while a singly quantized vortex is created in that of component 2 (see Fig. 5(e)). When the SOC is further enhanced, the number of vortices increases, the two components gradually change from complete phase separation to phase mixing, and the system finally forms a wheel-like delaminated vortex necklace, which is displayed in Figs. 5(f)–5(h). Note that the large density hole in Fig. 5(h) denotes a giant vortex plus hidden vortex necklace(s) rather than a pure giant vortex which is observed in conventional rotating BECs.[50] Physically, when the SOC strength increases with fixed other parameters, more angular momentum contributes to the system and leads to the generation of more vortices. Furthermore, the stronger the interspecies interaction is, the more angular momentum is input due to the presence of SOC and rotation, so the more vortices are generated.

It is worth mentioning that the exact ground state of a rotating two-component BEC with SOC in a toroidal trap[35] can not be determined simply by the density and momentum distributions of the two components. To accurately determine the topological structures of density holes in the density distributions, the phase distributions must also be examined, which is evidently indicated in Figs. 5(d), 5(e), and 5(h). In experiments, the various ground-state structures for the present system should be readily distinguished and observed by monitoring *in situ* the density profile and using the time-of-flight imaging.

3.3. The effect of rotation

Now we consider the effect of rotation on the ground state of the system with fixed DDI and SOC strengths. The typical density distributions, phase distributions, total densities, and density differences are displayed in Fig. 6. As shown in Fig. 6(a), in the absence of rotation, it is found that the system displays obvious petal-like phase separation (component separation) with few ghost vortices and antivortices being generated in each component, which is different from the annular segregated phase of a non-rotating spin–orbit-coupled BEC in a harmonic trap.[30] When $\Omega = 0.3$, the system exhibits a peculiar triangular vortex lattice with QDs (see Fig. 6(b)),[38–40] where three distinct QDs in component 2 are arranged in a triangle. At the same time, a standard triangular vortex lattice appears in component 1 while a hidden triangular vortex lattice surrounded by a hidden triangular antivortex lattice emerges in component 2. As the rotation frequency increases to $\Omega = 0.5$, the system displays a novel square vortex lattice with four QDs in component 2 (see Fig. 6(c)). Here the five vortices in component 1 are arranged into a criss-cross vortex string lattice, and the four hidden vortices in component 2 constitute a square vortex lattice. For the case of $\Omega = 1$ (Fig. 6(d)), the visible vortices in each component form a vortex necklace and the QDs in component 2 develop into a necklace structure. The large density hole in component 1 corresponds to a hidden square vortex lattice made of four hidden singly quantized vortices (not a conventional giant vortex), while that in component 2 is a triply quantized giant vortex. For large rotation frequency $\Omega = 1.4$, the QDs disappear, and the two components become miscible. The system shows an obvious vortex necklace structure, and each component contains a giant vortex in the center (see Fig. 6(e)). With the further increase of the rotation frequency, the system supports a vortex necklace (or vortex necklaces) in each component which is accompanied by a hidden giant vortex plus a (several) hidden vortex necklace(s) in the central region (not shown here for brevity). Particularly, the topological defects in Figs. 6(a)–6(c) are typical Anderson–Toulouse coreless vortices[51] because there are no singular points in the total density $|\psi_1|^2 + |\psi_2|^2$ of the system, whereas those in Figs. 6(d) and 6(e) are nucleated vortices as there are obvious singular points in the total density.

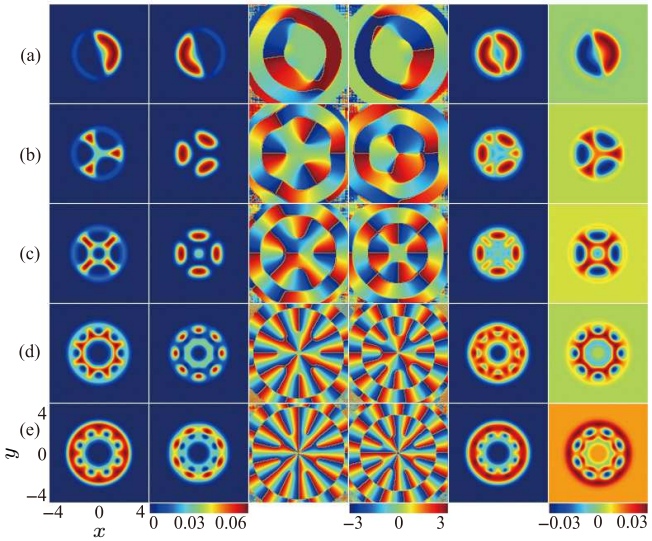


Fig. 6. Ground states of rotating spin-1/2 BECs with SOC and DDI in a toroidal trap, where $\gamma_{dd} = 0.5$, $\lambda = 2$, and $\delta = 7.5$. (a) $\Omega = 0$, (b) $\Omega = 0.3$, (c) $\Omega = 0.5$, (d) $\Omega = 1$, and (e) $\Omega = 1.4$. The rows from left to right represent $|\psi_1|^2$, $|\psi_2|^2$, $\arg\psi_1$, $\arg\psi_2$, $|\psi_1|^2 + |\psi_2|^2$, and $|\psi_1|^2 - |\psi_2|^2$, respectively. The unit length is a_0.

From Fig. 6, the increase of the rotation frequency can trigger the structural phase transition of the system and the transition from component separation to component mixing. Our simulation shows that the quantum droplets in Figs. 6(b)–6(d) are mainly attributed to the competition between DDI, contact interaction and the toroidal confinement. When the rotation frequency is small, the DDI effect and the SOC effect are dominant in determining the ground state of the system, but with the increase of the rotation frequency, the rotation effect gradually becomes dominant. The exotic topological structures in Figs. 2 and 4–6 (especially the

various-shaped vortex lattices with QDs shown in Figs. 2(b), 2(c), 4(a), 4(d), 5(b), 5(e), and 6(b)–6(e)) are evidently different from the ground-state configurations in conventional SOC BECs,[12,14,21,25,26,36] dipolar BECs,[6] and rotating two-component BECs with or without SOC (DDI).[27,28,30,35,42,50] Based on the above analysis and discussion, four important parameters, the SOC, DDI, rotation, and toroidal trap can be used to obtain the desired ground-state phases and to control the phase transition between various ground states of BECs. Considering the four important parameters of SOC, DDI, rotation, and toroidal trap, we summarize the typical ground-state phases of two-component BECs in Table 1, where the quantum phases without references are our simulation results.

Table 1. Typical ground-state phases of two-component BECs.

Case	Ground-state phase
$S_0D_0R_0T_0$	Mixing phase or demixing phase[52]
$S_0D_0R_0T_1$	Quantized persistent flow[34]
$S_0D_0R_1T_0$	Triangular vortex lattice[50]
$S_0D_0R_1T_1$	Giant vortex[22,43]
$S_0D_1R_0T_0$	Rosensweig pattern[2]
$S_0D_1R_0T_1$	Layer-separated symmetry preserving annular structure[53]
$S_1D_0R_0T_0$	Plane-wave phase or stripe phase[14,21]
$S_1D_0R_0T_1$	Necklace state[36]
$S_0D_1R_1T_0$	Half-quantum vortex chain phase[54]
$S_0D_1R_1T_1$	Symmetry broken separated phase
$S_1D_0R_1T_0$	Half-quantum vortex[27]
$S_1D_0R_1T_1$	Vortex necklace with hidden giant vortex and hidden vortex necklaces[22]
$S_1D_1R_0T_0$	Immiscible phase with hidden vortex, or plane-wave phase[55]
$S_1D_1R_0T_1$	Petal-like separated phase with ghost vortices and antivortices in each component
$S_1D_1R_1T_0$	Vortex sheet
$S_1D_1R_1T_1$	Symmetrical (asymmetrical) phase with QDs, vortex lattice with QDs, and criss-cross vortex string lattice, etc

Here S_0 (D_0 and R_0) indicates that there is no SOC (DDI and rotation) in the system, and S_1 (D_1 and R_1) means that there is SOC (DDI and rotation) in the system. T_0 represents that the BECs are homogeneous or confined in a harmonic trap, while T_1 denotes that the BECs are confined in a toroidal trap. The ground-state phases without references are our simulation results.

3.4. Spin densities and spin textures

In order to further shed light on the ground-state properties, we analyze the spin densities and spin textures of the system. The representative density differences $|\psi_1|^2 - |\psi_2|^2$ and spin density distributions are shown in Fig. 7, where the density and phase distributions corresponding to Figs. 7(a)–7(d) are given in Figs. 2(b), 4(e), 5(a), and 5(d), respectively. In the pseudo-spin representation, the red region denotes spin-up and the blue region denotes spin-down. Considering the correlation between density difference and spin component S_z, we also present the density differences in the top row. From Figs. 7(a), 7(b), and 7(d), S_x obeys an odd-parity distribution along the x direction and an even-parity distribution along the y direction, while the situation is reverse for S_y. At the same time, S_z satisfies an even-parity distribution along both the x and the y directions. Of particular interest is Fig. 7(c), where S_x and S_z obey an even-parity along the y direction, S_y satisfies an odd-parity along the y direction, but there is no symmetry with respect to the $x = 0$ axis (i.e., along the x direction) for S_x, S_y, and S_z. In addition, the spin component S_z develops into two distinct spin domains due to the component separation of the two component densities, and the boundary between the two spin domains forms a peculiar trumpet-shaped spin domain wall with $|S_z| \neq 1$, which can be seen clearly in the bottom panel of Fig. 7(c). It is well known that the spin domain wall for non-rotating two-component BECs is a classical Néel wall, where the spin flips only along the vertical direction of the wall. However, our numerical simulation demonstrates that the spin in the region

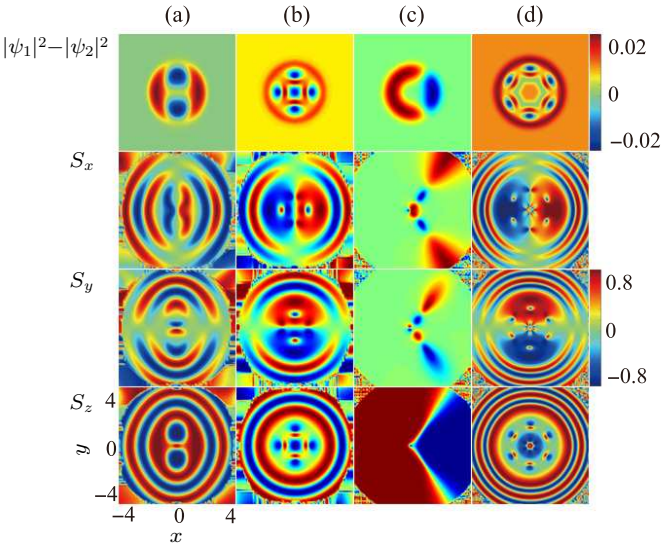


Fig. 7. Density differences and spin densities of rotating spin-1/2 BECs with SOC and DDI in a toroidal trap. The rows from top to bottom denote $|\psi_1|^2 - |\psi_2|^2$, S_x, S_y, and S_z, respectively. The corresponding ground states in (a)-(d) are shown in Figs. 2(b), 4(e), 5(a), and 5(d), respectively. The unit length is a_0.

of spin domain wall flips not only along the vertical direction of the domain wall but also along the domain-wall direction, which implies that the observed domain wall is a unique Bloch wall instead of a common Néel wall.

The present system sustains not only the line-like topological excitation (vortex excitation) concerning the spatial degrees of freedom of the condensates but also the point-like topological excitation (skyrmion excitation) with respect to the spin degrees of freedom. Shown in the left two columns of Fig. 8 are the typical topological charge densities (column 1) and the spin textures (column 2) of the system, where the ground states for Figs. 8(a)–8(d) are given in Figs. 2(b), 4(c), 4(d), and 4(e), respectively. The corresponding local amplifications of the spin textures are presented in the right two columns of Fig.8. In Fig. 9, we display the topological charge densities, the spin textures, and the local enlargements of the spin textures for the parameters in Figs. 5(a), 5(d), 5(f), and 6(e), respectively. For the convenience of discussion, we use red solid square, red solid circle, red solid octagon, and blue dotted circle to denote a skyrmion, a half-skyrmion, a giant skyrmion, and a half-antiskyrmion, respectively.

Our numerical calculation shows that the local topological charges in Figs. 8(a3) and 8(a4) approach $Q = 0.5$, which indicates that the local topological defects in Figs. 8(a3) and 8(a4) are hyperbolic half-skyrmion (meron) and radial(out) half-skyrmion,[29,45,56,57] respectively. Thus the spin texture in Fig. 8(a2) forms a special half-skyrmion (meron) string along the y direction composed of a hyperbolic half-skyrmion in the center and two symmetric radial(out) half-skyrmions in the two sides. Shown in the spin texture of Fig. 8(b2) is a typical hyperbolic-radial(out) skyrmion[29] with unit topological charge $Q = 1$, and the local amplifications are given in Figs. 8(b3) and 8(b4). From Figs. 8(c2)–8(c4), we can see that there are three radial(out) skyrmions with respective topological charge $Q = 1$ and they are arranged in an equilateral triangle. Therefore the spin defect in Fig. 8(c2) is a triangular radial(out) skyrmion lattice. In particular, the topological charge density in Fig. 8(d1) displays a petal-like structure consisting of four evident criss-cross petals and an inconspicuous torus in the center of the toroidal trap. Figure 8(d2) is

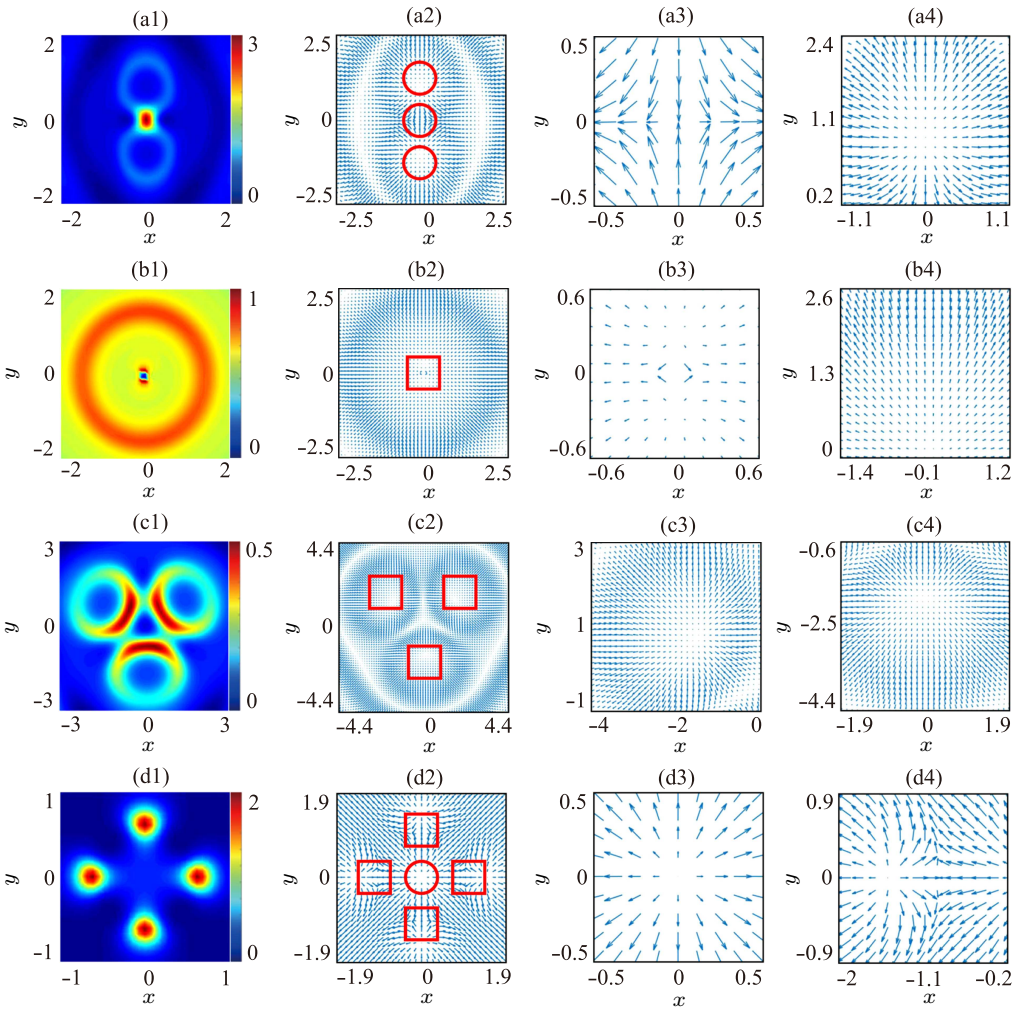


Fig. 8. Topological charge densities and spin textures of spin–orbit-coupled dipolar BECs in a rotating toroidal trap, where the corresponding ground states for (a)–(d) are given in Figs. 2(b), 4(c), 4(d), and 4(e), respectively. The first column (from left to right) represents topological charge density, the second column is spin texture, and the right two columns denote the local amplifications of the spin texture. The red solid square and the red solid circle denote a skyrmion and a half-skyrmion, respectively. The unit length is a_0.

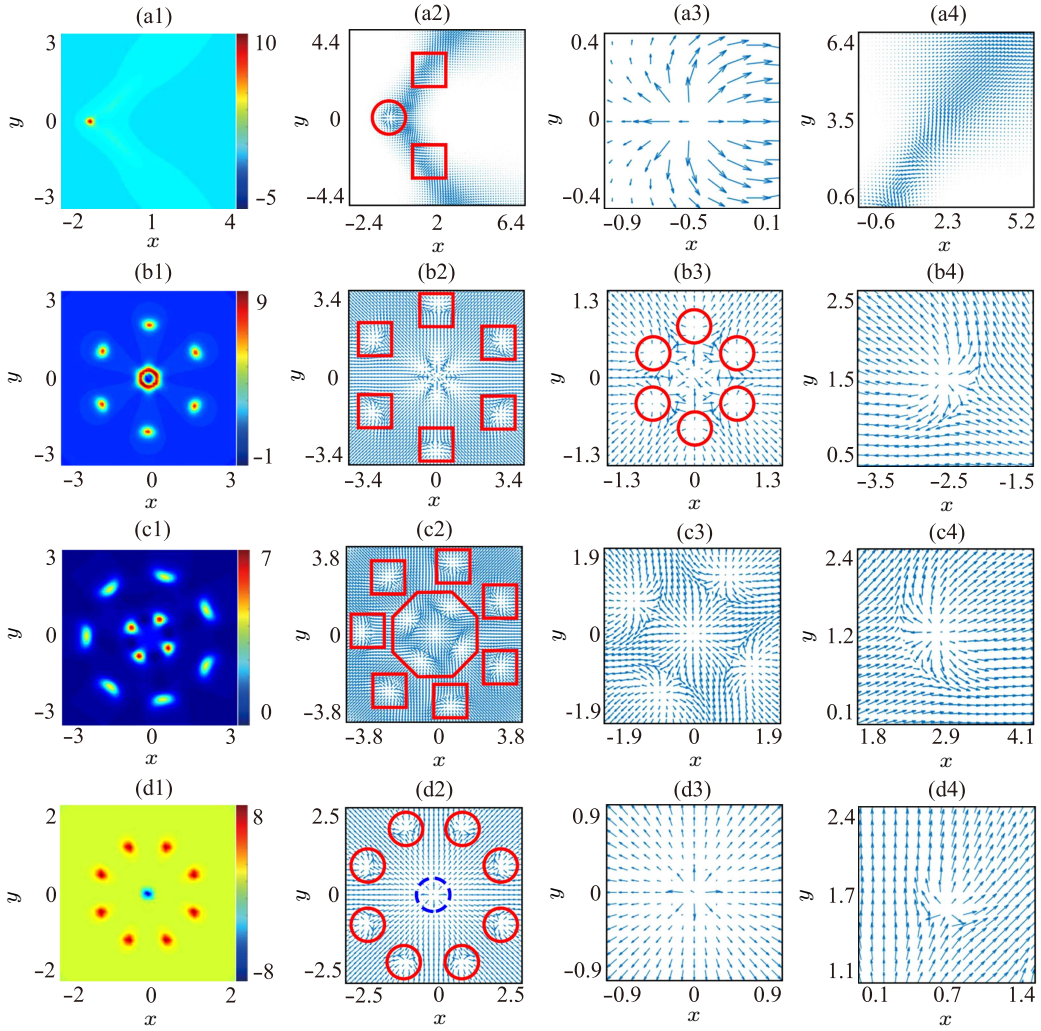


Fig. 9. Topological charge densities and spin textures of spin–orbit-coupled dipolar BECs in a rotating toroidal trap, where the ground states for (a)–(d) are shown in Figs. 5(a), 5(d), 5(f), and 6(e), respectively. The first column (from left to right) denotes topological charge density, the second column is spin texture, and the right two columns represent the local amplifications of the spin texture. The red solid square, red solid circle, red solid octagon, and blue dotted circle represent a skyrmion, a half-skyrmion, a giant skyrmion, and a half-antiskyrmion, respectively. The unit length is a_0.

the corresponding spin texture, where the local enlargements are shown in Figs. 8(d3) and 8(d4), and the local topological charges are $Q = 0.5$ and $Q = 1$, respectively. The four skyrmions and a half-skyrmion (meron) in Fig. 8(d2) compose an exotic skyrmion-half-skyrmion (skyrmion-meron) lattice in which the outer four spin defects are hyperbolic-radial(out) skyrmions and the central spin defect is a radial(out) half-skyrmion (meron).

The topological charge densities and spin textures in Fig. 9 are richer and more interesting, where the ground states are displayed in Figs. 5(a), 5(d), 5(f), and 6(e). Our computation results show that the local topological charges in Figs. 9(a3) and 9(a4) are $Q = 0.5$ and $Q = 1$, respectively. This indicates that the spin texture in Fig. 9(a2) is a trumpet-shaped skyrmion-half-skyrmion cluster composed of a half-skyrmion and two skyrmions. Considering Fig. 9(b1), we see that the topological charge density has good discrete rotational symmetry. The six density peaks are evenly arranged along a circle and a hexagonal density profile is located in the central region. The excellent symmetry is also embodied in the spin texture of Fig. 9(b2), where typical local amplifications are illustrated in Figs. 9(b3) and 9(b4). From Figs. 9(b2)–9(b4), there are six hyperbolic-radial(out) skyrmions with respective local topological charge $Q = 1$, and they form an obvious skyrmion necklace along a large circle. In the mean time, a half-skyrmion (meron) necklace consisting of six radial(out) half-skyrmions with respective local topological charge $Q = 0.5$ is generated around the trap center. Therefore, the topological structure of the system is a complex skyrmion–half-skyrmion layered necklace composed of an outer skyrmion necklace and an inner half-skyrmion necklace. Figure 9(c3) is the local amplification of the octagonal region in Fig. 9(c2), which is a giant skyrmion with topological charge $Q = 4$. At the same time, the local topological charge in Fig. 9(c4) is $Q = 1$. Thus the spin texture in Fig. 9(c2) denotes a peculiar skyrmion–giant-skyrmion necklace lattice. Similar analysis shows that the local spin defect in Fig. 9(d3) is a radial(out) half-antiskyrmion with topological charge $Q = -0.5$. Furthermore, our calcu-

lation result shows that the local amplification in Fig. 9(d4) corresponds to a radial(out) half-skyrmion with topological charge $Q = 0.5$, and such eight half-skyrmions constitute a half-skyrmion necklace. Hence the topological structure in Fig. 9(d2) is an exotic half-skyrmion–half-antiskyrmion necklace. Obviously, most of the skyrmion excitations observed in the present system are remarkably different from the previously reported ones in rotating two-component BECs with or without SOC (DDI),[18,26–28,30,35,42,50] and can be tested and observed in future experiments.

4. Conclusion

In summary, we have studied the topological excitations of spin-1/2 BECs with SOC and DDI in a rotating 2D toroidal trap. The combined effects of DDI, SOC, rotation, interatomic interactions, and toroidal trap on the ground-state structures and topological defects of the system are discussed systematically. Our results show that the DDI and SOC play a key role in determining the ground-state phase of the system for the case of small rotation frequency, while for the case of large rotation frequency, the rotation effect becomes dominant. Two ground-state phase diagrams for fixed SOC strength and rotation frequency are given with respect to the DDI strength and the ratio between inter- and intra-species interactions. The system can show a rich variety of ground-state phases such as HQV phase, SQD phase, ASH phase, ACG phase, TVD phase, SVD phase, CVS phase, TVL phase, and vortex necklace with hidden vortices, depending on the complex competition among the DDI, SOC, rotation, interatomic interactions, and the toroidal confinement. In the absence of rotation, the interplay between DDI and SOC may lead to the formation of a unique trumpet-shaped spin Bloch domain wall. In addition, the system sustains exotic new topological defects including a half-skyrmion (meron) string, triangular radial(out) skyrmion lattice, skyrmion–half-skyrmion lattice, skyrmion–meron cluster, skyrmion–meron layered necklace, skyrmion–giant-skyrmion necklace lattice, and half-skyrmion–half-antiskyrmion necklace. Furthermore, as four important degrees of freedom, the DDI, SOC, rotation, and contact interaction can be used to achieve the desired ground-state phases and to control the phase transition between various ground states of BECs in a toroidal trap. The findings in the present work have enriched our new understanding for topological excitations in cold atom physics and condensed matter physics.

Acknowledgment

LHW acknowledges the research group of Professor W. Vincent Liu at The University of Pittsburgh (UP), where part of the work was carried out during his visit to UP.

References

[1] Lahaye T, Menotti C, Santos L, Lewenstein M and Pfau T 2009 *Rep. Prog. Phys.* **72** 126401
[2] Kawaguchi Y and Ueda M 2012 *Phys. Rep.* **520** 253
[3] Santos L, Shlyapnikov G V and Lewenstein M 2003 *Phys. Rev. Lett.* **90** 250403
[4] Deng Y, Cheng J, Jing H, Sun C P and Yi S 2012 *Phys. Rev. Lett.* **108** 125301
[5] Kadau H, Schmitt M, Wenzel M, Wink C, Maier T, Ferrier-Barbut I and Pfau T 2016 *Nature* **530** 194
[6] Prasad S B, Bland T, Mulkerin B C, Parker N G and Martin A M 2019 *Phys. Rev. A* **100** 023625
[7] Oldziejewski R, Gorecki W, Pawlowski K and Rzazewski K 2020 *Phys. Rev. Lett.* **124** 090401
[8] Lepoutre S, Gabardos L, Kechadi K, Pedri P, Gorceix O, Maréchal E, Vernac L and Laburthe-Tolra B 2018 *Phys. Rev. Lett.* **121** 013201
[9] Lu M, Burdick N Q, Youn S H and Lev B L 2011 *Phys. Rev. Lett.* **107** 190401
[10] Chomaz L, van Bijnen R M W, Petter D, Faraoni G, Baier S, Becher J H, Mark M J, Wächtler F, Santos L and Ferlaino F 2018 *Nat. Phys.* **14** 442
[11] Christianen A, Zwierlein M W, Groenenboom G C and Karman T 2019 *Phys. Rev. Lett.* **123** 123402
[12] Lin Y J, Jiménez-GarcíaK K and Spielman I B 2011 *Nature* **471** 83
[13] Cheuk L W, Sommer A T, Hadzibabic Z, Yefsah T, Bakr W S and Zwierlein M W 2012 *Phys. Rev. Lett.* **109** 095302
[14] Zhai H 2015 *Rep. Prog. Phys.* **78** 026001
[15] Bychkov Y A and Rashba E I 1984 *J. Phys. C* **17** 6039
[16] Dresselhaus G 1955 *Phys. Rev.* **100** 580
[17] Goldman N, Juzeliūnas G, Öhberg P and Spielman I B 2014 *Rep. Prog. Phys.* **77** 126401
[18] Yang H, Wang Q, Su N and Wen L 2019 *Eur. Phys. J. Plus* **134** 589
[19] Wu Z, Zhang L, Sun W, Xu X T, Wang B Z, Ji S C, Deng Y, Chen S, Liu X J and Pan J W 2016 *Science* **354** 83
[20] Huang L, Meng Z, Wang P, Peng P, Zhang S L, Chen L, Li D, Zhou Q and Zhang J 2016 *Nat. Phys.* **12** 540
[21] Zhang Y, Mao L and Zhang C 2012 *Phys. Rev. Lett.* **108** 035302
[22] Wang H, Wen L, Yang H, Shi C and Li J 2017 *J. Phys. B* **50** 155301
[23] Li J R, Lee J, Huang W, Burchesky S, Shteynas B, Top F C, Jamison A O and Ketterle W 2017 *Nature* **543** 91
[24] Xu Y, Zhang Y and Wu B 2013 *Phys. Rev. A* **87** 013614
[25] Sinha S, Nath R and Santos L 2011 *Phys. Rev. Lett.* **107** 270401
[26] Hu H, Ramachandhran B, Pu H and Liu X J 2012 *Phys. Rev. Lett.* **108** 010402
[27] Xu X Q and Han J H 2011 *Phys. Rev. Lett.* **107** 200401
[28] Zhou X F, Zhou J and Wu C 2011 *Phys. Rev. A* **84** 063624
[29] Liu C F, Fan H, Zhang Y C, Wang D S and Liu W M 2012 *Phys. Rev. A* **86** 053616
[30] Aftalion A and Mason P 2013 *Phys. Rev. A* **88** 023610
[31] Wen L, Xiong H and Wu B 2010 *Phys. Rev. A* **82**, 053627
[32] Wei Y W, Kong C and Hai W H 2019 *Chin. Phys. B* **28** 056701
[33] Zhang A X, Zhang Y, Jiang Y F, Yu Z F, Cai L X and Xue J K 2020 *Chin. Phys. B* **29** 010307
[34] Eckel S, Lee J G, Jendrzejewski F, Murray N, Clark C W, Lobb C J, Phillips W D, Edwards M and Campbell G K 2014 *Nature* **506** 200
[35] Zhang X F, Kato M, Han W, Zhang S G and Saito H 2017 *Phys. Rev. A* **95** 033620
[36] White A C, Zhang Y P and Busch T 2017 *Phys. Rev. A* **95** 041604
[37] Li J, Liu B, Bai J, Wang H Y and He T C 2020 *Acta Phys. Sin.* **69** 140301 (in Chinese)
[38] Mason P and Aftalion A 2011 *Phys. Rev. A* **84** 033611
[39] Cabrera C R, Tanzi L, Sanz J, Naylor B, Thomas P, Cheiney P and Tarruell L 2018 *Science* **359** 301
[40] Cui X 2018 *Phys. Rev. A* **98** 023630
[41] Adhikari S K 2014 *Phys. Rev. A* **89** 013630
[42] Zhang X F, Han W, Jiang H F, Liu W M, Saito H and Zhang S G 2016 *Ann. Phys.* **375** 368
[43] Cozzini M, Jackson B and Stringari S 2006 *Phys. Rev. A* **73** 013603

[44] Shirley W E, Anderson B M, Clark C W and Wilson R M 2014 *Phys. Rev. Lett.* **113** 165301
[45] Kasamatsu K, Tsubota M and Ueda M 2005 *Phys. Rev. A* **71** 043611
[46] Wen L, Qiao Y, Xu Y and Mao L 2013 *Phys. Rev. A* **87** 033604
[47] Wen L and Li J 2014 *Phys. Rev. A* **90** 053621
[48] Ferrier-Barbut I, Wenzel M, Boettcher F, Langen T, Isoard M, Stringari S and Pfau T 2018 *Phys. Rev. Lett.* **120** 160402
[49] Tang Y, Sykes A, Burdick N Q, Bohn J L and Lev B L 2015 *Phys. Rev. A* **92** 022703
[50] Fetter A L 2009 *Rev. Mod. Phys.* **81** 647
[51] Anderson P W and Toulouse G 1977 *Phys. Rev. Lett.* **38** 508
[52] Pethick C J and Smith H 2008 *Bose–Einstein Condensation in Dilute Gases*, 2nd edn. (New York: Cambridge University Press) pp. 348–354
[53] Yang H, Wang Q and Wen L 2019 *J. Phys. Soc. Jpn.* **88** 064001
[54] Shirley W E, Anderson B M, Clark C W and Wilson R M 2014 *Phys. Rev. Lett.* **113** 165301
[55] Li X, Wang Q, Wang H, Shi C, Jardine M and Wen L 2019 *J. Phys. B* **52** 155302
[56] Skyrme T H R 1962 *Nucl. Phys.* **31** 556
[57] Mermin N D and Ho T L 1976 *Phys. Rev. Lett.* **36** 594